Steady-state aeroelasticity of a ram-air wing for airborne wind energy applications

Folkersma, Mikko; Schmehl, Roland; Viré, Axelle

DOI
10.1088/1742-6596/1618/3/032018

Publication date
2020

Document Version
Final published version

Published in
Journal of Physics: Conference Series

Steady-state aeroelasticity of a ram-air wing for airborne wind energy applications

Steady-state aeroelasticity of a ram-air wing for airborne wind energy applications

Mikko Folkersma, Roland Schmehl, and Axelle Viré

Faculty of Aerospace Engineering, Delft University of Technology, Kluyverweg 1, 2629 HS Delft, The Netherlands

E-mail: m.a.m.folkersma@tudelft.nl

Abstract. In this paper we present a computational approach to simulate the steady-state aeroelastic deformation of a ram-air kite for airborne wind energy applications. The approach is based on a computational fluid dynamics (CFD) solver that is two-way coupled with a finite element (FE) solver. All components of the framework, including the meshing tools and the coupling library, are available in open source. The flow around the wing is described by the steady-state Reynolds-averaged Navier-Stokes (RANS) equations closed by an SST turbulence model. The FE model of the cellular membrane structure includes a wrinkling model and uses dynamic relaxation to find the deformed steady-state shape. Each simulation comprises four distinct steps: (1) generating the FE mesh of the design geometry, (2) pre-inflation of the wing, applying a uniform pressure on the inside, (3) generating the CFD mesh around the pre-inflated wing, and (4) activating the exterior flow and two-way coupling iterations. We first present results for the aerodynamics of the pre-inflated rigid ram-air wing and compare these to similar results for a leading edge inflatable (LEI) tube kite. Both wings are characterized by a high anhedral angle and low aspect ratio which induce spanwise flows that reduce the aerodynamic performance. The comparison shows a better performance for the LEI wing which can be attributed to its higher aspect ratio. The aeroelastic deformation of the ram-air wing further improves the aerodynamic performance, primarily because of the increasing camber which in turn increases the lift force. A competing aeroelastic phenomenon is the formation of bumps near the leading edge which increase the drag.

1. Introduction

Airborne wind energy (AWE) is a novel wind energy concept employing tethered flying devices to harvest energy at higher altitudes. The lightweight structures are expected to significantly reduce the cost of energy and because the flight operation can be adjusted easily to a varying wind resource, the energy availability increases in comparison to conventional wind turbines. However, the use of a tensile structure and flying component also poses essential challenges for robust and continuous long-term operation in an unsteady and turbulent wind field. A widely pursued AWE concept uses the pulling force of a wing and converts this into electricity with a drum-generator module on the ground. For continuous energy generation, these systems are operated in consecutive pumping cycles, alternating between reel out and reel in of the tether. During tether reel-out, the wing is flown in fast crosswind maneuvers, at high angle of attack, to generate a high lift force and thus high tether force to drive the generator. During tether reel in, the tether tension is minimized by discontinuing the crosswind maneuvers and actively reducing the aerodynamic lift of the wing.

In the present work, we focus on ram-air wings, which are designed as cellular membrane structures inflated by the exterior flow through openings on the leading edge [10, 16]. The distributed aerodynamic load on the top and bottom skin of the wing is collected by membrane ribs and from there transmitted to the main tether via fans of bridle lines. By design, tethered ram-air wings are characterized by a strong coupling of flight dynamics, aerodynamics and structural dynamics. The inflation pressure acting on the inside of the cellular structure depends quadratically on the relative flow speed and for fast-flying wings this is close to the flight speed of the wing. The aerodynamic force distribution acting on the outside of the structure also scales with the square of the relative flow speed, yet, it additionally depends on the orientation of the wing with respect to the flow. In difference to conventional wing materials, a fabric membrane can not sustain any bending moment and as consequence, the cellular structure deforms until the aerodynamic force distribution on the outside and the uniform pressure on the inside are in steady equilibrium with the tensile forces in the membrane and the bridle line forces acting in the attachment points. This shape adjustment in turn affects the exterior flow field and by that the aerodynamic force distribution and its resultant, which again controls the flight speed of the tethered wing.

While the aerodynamics and structural dynamics of ram-air wings for para-gliding have been studied in great detail using computational fluid dynamics and finite element analyses [6, 14, 15, 1], only few studies have considered ram-air wings for wind energy harvesting. De Wachter [8] has used photogrammetry and laser scanning to measure the three-dimensional shape of small ram-air wings in wind tunnels to use this shape in a second step for detailed CFD analyses. In a parallel study, Bungart [4] has solved the fluid-structure interaction problem numerically, also solving for the deformation of the wing as a result of the aerodynamic loading. In the present study, we account for the aeroelasticity of a ram-air wing for AWE applications by two-way coupling an aerodynamics solver to a structural mechanics solver. The problem is assumed to lead to a steady flow and deformation state. We do not simulate the flow inside the wing but instead assume a constant inflation pressure that we apply in a pre-simulation of the cellular membrane structure. Previous work focused on developing the methodology by simulating a single-cell ram-air wing [13]. The present study extends this work by simulating the full three-dimensional kite including the bridle line system. We also compare these results with a parallel computational analysis of a leading edge inflatable (LEI) kite [20].

The paper is organized as follows. Section 2 introduces the three main components of the coupled framework: the aerodynamic solver, the structural solver and the coupling tool. Also, a separate subsection is dedicated to the major challenge in CFD, the mesh generation. Section 3 presents the results of the framework around the rigid pre-inflated shape of the kite and the aeroelastic kite. The paper is concluded in Section 4.

2. Methodology

The computational methodology comprises four successive steps. First, surface and line meshes are generated from the design geometry and bridle line system of the wing. In a second step, we determine the inflated shape in a pre-simulation, applying a uniform pressure inside the cellular membrane structure. In a third step, the volume mesh is generated around the surface mesh and in the last step, the full aeroelastic problem is solved by two-way coupled iterations alternating between FE and CFD solvers until a steady converged wing shape and flow field is reached. The design geometry of the wing and the bridle lines as well as the surface mesh are illustrated in 1. Key geometry parameters are listed in Table 1. In this section, we outline the main components of the computational methodology. All the software tools used in this work are available as free and open-source software.

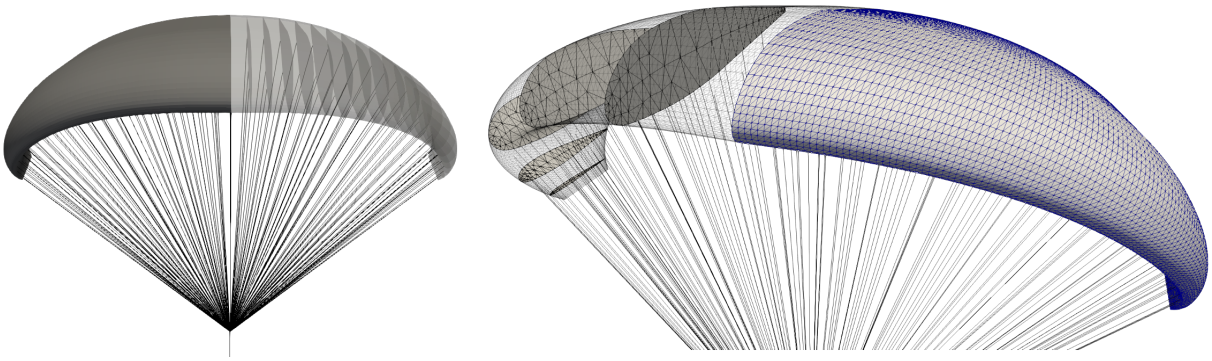

Figure 1. Initial design shape of the kite (left) and surface mesh discretizing the cellular wing structure, consisting of top and bottom skin and membrane ribs (right).

Table 1. Key geometry parameters of the kite.

Parameter	Symbol and definition	Value
Total surface area	A	160 m^2
Projected surface area	S	125 m^2
Projected span	b	15.2 m
Projected aspect ratio	$AR = b^2/S$	1.86
Maximum chord	$c_{\max}$	9.26 m

2.1. Aerodynamic model

The exterior flow field is calculated with the OpenFOAM v1906 CFD toolbox. OpenFOAM uses an unstructured finite-volume discretization of the incompressible Navier-Stokes equations. We use the steady-state solver which is based on the classic SIMPLE algorithm and RANS turbulence modeling with a shear-stress transport (SST) turbulence model. The spatial discretization schemes are second order upwind for momentum and first order upwind for turbulence quantities (k and ω). The convergence criteria for the residuals are set to 10^{-6}. The computational domain extends 100 chord lengths from the kite in all directions and forms a sphere. A mixed boundary condition is used at the far field, which switches between Dirichlet and Neumann boundary conditions depending on the direction of the local flow (inlet and outlet). No wall functions are used in the simulations and therefore the dimensionless wall distance of the first cell $y+$ is less than unity everywhere. The bridle line system is not taken into account in the exterior flow model. The key parameters for the CFD simulations are given in Table 2.

Table 2. Key parameters of the CFD simulation.

Parameter	Symbol and definition	Value
Reynolds number	$\mathrm{Re} = U c_{\max}/\nu$	5×10^6
Dynamic pressure	$p_0 = \frac{1}{2}\rho_\mathrm{f} U^2$	540 Pa
Turbulence intensity	I	2%
Eddy viscosity ratio	ν_t/ν	10

2.2. Structural model

The deformation of the aerodynamically loaded structure is calculated with the FE solver mem4py, which is specifically developed for thin membrane structures [19, 18]. The membrane

elements are zero thickness triangle elements which cannot resist any bending. A wrinkling model is used when an element is under compression. The bridle lines are discretized by concatenated two-noded tension-only cable elements. The aerodynamic line drag is taken into account using a simplified force model [11]. The material model for the membrane and cable elements is isotropic linear elastic. The solver uses a dynamic relaxation method to find the steady-state shape of the kite. The structural parameters of the simulation are given in Table 3.

Table 3. Key parameters of the structural simulation.

Parameter	Symbol and definition	Value
Inflation over pressure	p_i	540 Pa
Membrane Young's modulus	$E_\mathrm{m} \times t$	10 kN/m
Membrane Poisson's ratio	ν_m	0.3
Bridle line Young's modulus	E_c	83.6 GPa
Bridle line diameter	d	2.5 mm

The geometry of the kite is illustrated in Figure 1. The wing is partitioned into 38 individual cells, which are defined by 39 ribs that are covered by a top and bottom skin membrane. The airfoil-shaped ribs define the aerodynamic shape of the wing and accordingly the wing geometry is generated by lofting through the rib airfoils. The top and the bottom skin of the wing and the ribs are made from the same membrane material. At the pressure side, each rib is supported by four bridle lines which converge into the main tether at the bridle point. The position of the bridle point relative to the wing and thus the lengths of the bridle lines control the trimming of the kite. Because of the expected low flow velocities, the flow inside the ram-air wing is not modelled but an uniform inflation pressure is applied. Moreover, the main tether and the gravitational forces are not taken into account.

2.3. Mesh generation

The mesh generation is often the most time consuming and challenging part of a CFD project. In this work, the mesh generation is done in three steps with three different tools. Firstly, a structured surface mesh is generated for the design shape of the wing with the Cassiopee pre- and post-processing tool [2]. The mesh is converted into a triangular mesh for the mem4py solver by splitting each quadrangle into two triangles. Additionally, the ribs are triangulated which results in a total of 17504 triangle elements. The structural solver calculates the pre-inflated shape using the triangular mesh and the computed displacements are mapped to the structured surface mesh. The structured surface mesh is further refined and stretched near the leading and the trailing edges to capture the high curvature for the requirements of the CFD simulation.

Secondly, the volume mesh close to the wing (red in Figure 2) is generated with the PyHyp [17] tool by extruding the surface mesh. PyHyp uses a hyperbolic extrusion algorithm for the extrusion which results in a nearly orthogonal mesh that is highly stretched in the wall normal direction to capture the boundary layer flow accurately with a minimal cell count. The deformed CFD mesh is smoothed slightly at the ribs of the wing to prevent self intersection. The mesh is extruded up to a thickness where the aspect ratio of the cells at the extrusion front are approximately unity. Thirdly, the rest of the domain is filled with a Cartesian mesh (gray in Figure 2) generated by the tool cfMesh, which is included in the OpenFOAM toolbox. The Cartesian mesh is refined near the wing and snapped at the interface of the boundary layer mesh with a layer of polyhedrons. The two meshes are not conforming at the common interface and, therefore, OpenFOAM's arbitrary mesh interface (AMI) is used to transport the quantities from one mesh to the other. The final volume mesh has around 5.7 million cells.

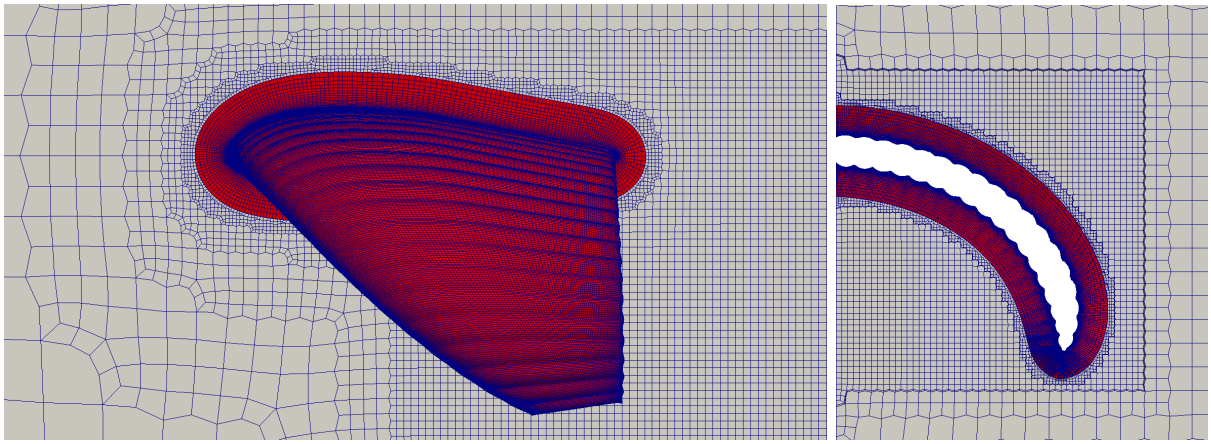

Figure 2. Volume mesh at the symmetry plane and at the the wing surface (left) and in streamwise direction at $x/c = 0.75$ (right). The colors show the two different regions of the mesh.

2.4. Aeroelastic coupling

The FE and CFD solvers are coupled with the preCICE [5] coupling tool, which handles the parallel communication between the solvers, the mapping of the exchanged quantities (forces and displacements) from one mesh to another and the coupling algorithm. Both solvers require an adapter for preCICE which can be developed in any of the main programming languages that preCICE supports. For instance, in this work the OpenFOAM adapter [7] is written in C++ and we have developed an adapter for the mem4py solver in its native language Python.

In the flow solver, the movement and deformation of the wing is taken into account by moving the membrane surface mesh and deforming the volumetric mesh accordingly. In the present work, we use the radial basis function (RBF) based mesh deformation library included in the FOAM-FSI package [3]. FOAM-FSI supports another version of OpenFOAM called foam-extend and therefore in the present work we have modified the RBF mesh deformation source code to work with the OpenFOAM v1906 toolbox [12]. In the aeroelastic coupling simulations, the angle of attack of the wing is controlled by trimming the bridle line system, moving the bridle point in streamwise direction and adjusting the lengths of the bridle lines accordingly. The effect of the initial streamwise position δ_x of the bridle point on the initial bridle geometry and the resulting equilibrium flight state is illustrated Figure 3 for two different trimming configurations. Trimming configuration 1, with position $\delta_{x,1}$ results in a low value α_1 of the steady-state angle of attack while configuration 2, with the bridle point shifted downstream to $\delta_{x,2}$, leads to a higher value α_2.

3. Results

We first inflate the wing and compute the flow around this pre-inflated shape, comparing this with a similar computational study for a leading edge inflatable (LEI) kite. Subsequently, the aeroelastic results are presented and compared against the rigid pre-inflated shape results to isolate the effect of the aeroelasticity.

3.1. Rigid pre-inflated kite

The inflated shape of the kite is calculated with the structural solver by imposing an uniform inflation pressure inside the wing. The cellular membrane structure balloons and forms the typical shape of a ram-air wing (Figure 1). The neighboring ribs move closer to each other and the upper and lower skin billow outwards which reduces the wing span. The membranes are

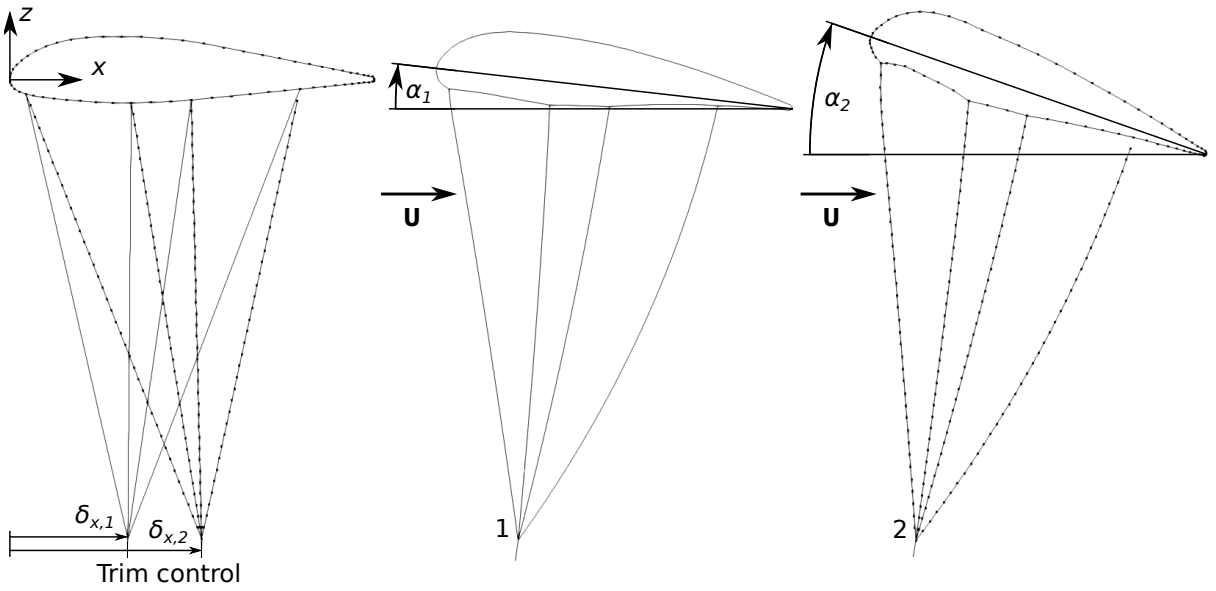

Figure 3. Trim configurations 1 and 2 for the design shape of the kite (left), and steady-state flight equilibrium (center & right) for the symmetry plane section of the kite.

made from relatively stiff material with negligible stretch. The CFD simulations are carried out for this rigid pre-inflated shape.

Figure 4 shows streamlines along the suction side of the rigid pre-inflated wing and the vorticity component ω_x in the wake flow. The low aspect ratio and the high anhedral angle of the wing lead to high spanwise flows and corresponding wingtip losses. The air leaks from the

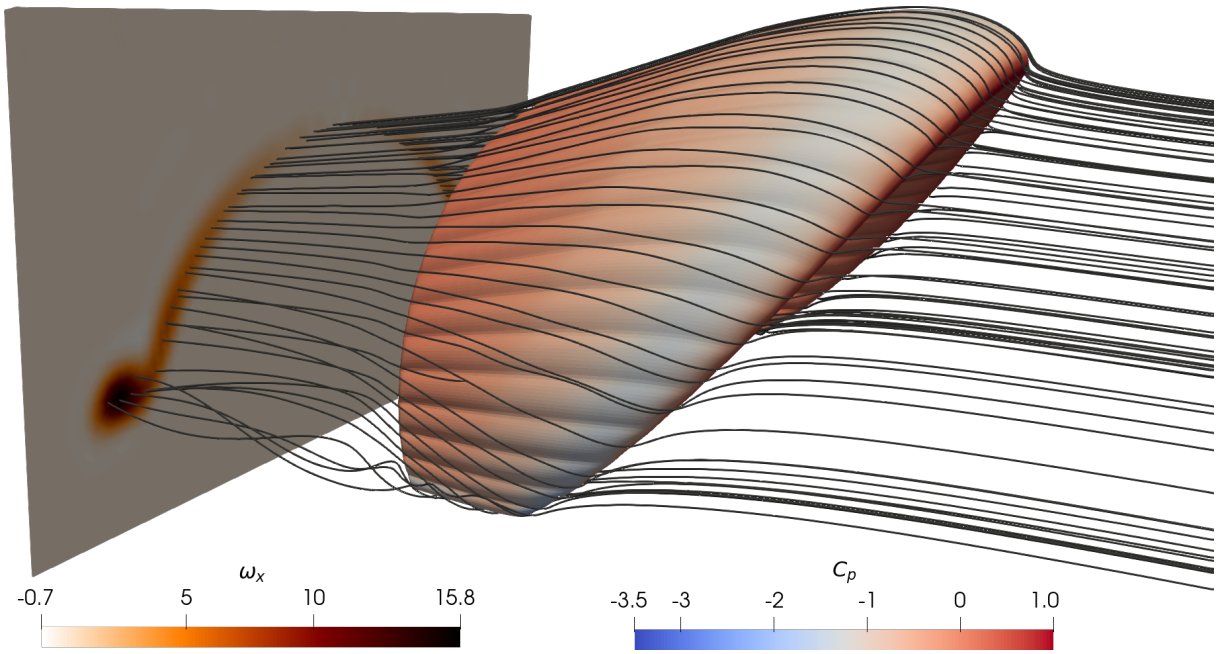

Figure 4. Streamlines along the suction side and vorticity component ω_x on a plane normal to the streamwise direction at $x = 1.5c$ and $\alpha = 10°$.

high pressure side to the suction side, which decreases the pressure difference between the two skins and results in a decreased lift force. On the upper skin of the wing, the spanwise flow pushes the streamlines towards the center of the wing. Additionally, wingtip vortices are formed in the wake which increase the drag force. The vortices are illustrated by the twisted streamlines and the peak in vorticity downstream of the wingtip.

The simulation results are compared with the results obtained by Demkowicz [9] and Viré et al. [20] for the flow around a rigid leading edge inflatable (LEI) kite at similar relative flow conditions. The lift and drag coefficients for both rigid wing shapes are shown in Figure 5. On first view, it is surprising that the aerodynamic performance of the LEI kite is consistently better across the entire range of angles of attack. One would expect, that a conventional airfoil, such as used for the present ram-air wing, has a better aerodynamic performance than a single skin LEI tube kite airfoil with an extended recirculation zone on the pressure side behind the leading edge tube. Figure 6 shows the front and planform views of the two different wings. Both have an anhedral angle of approximately 90° but the projected aspect ratio $AR = 3.49$ of the LEI kite is nearly two times higher than the aspect ratio $AR = 1.86$ of the ram-air kite. This geometric parameter generally increases the aerodynamic performance of a complete wing by decreasing the relative effect of the wingtip losses. This appears to be the main reason for the better aerodynamic performance of the LEI kite.

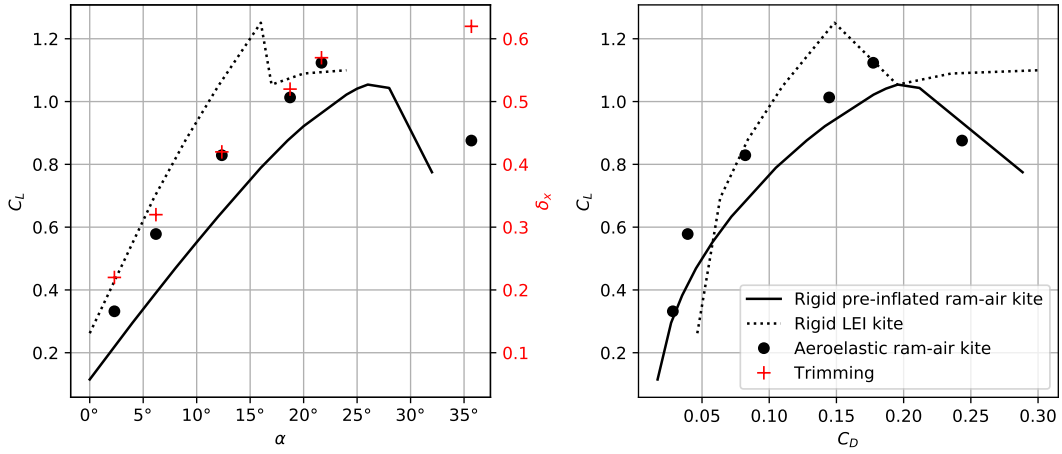

Figure 5. Lift (left) and drag (right) polars for the present ram-air kite and the LEI kite by Viré et al. [20].

3.2. Aeroelastic kite

The two-way coupling iterations are continued until the computed aerodynamic coefficients converge on constant values. The coefficients after each coupling step are shown in Figure 7. The coupled solver requires approximately 10 coupling steps to converge. A faster convergence could likely be achieved by using a more sophisticated coupling scheme than the weak coupling scheme used in this work. The simulations are carried out on a high performance computer using 8 cores. Each simulation takes around 10 hours of wall time resulting in 80 hours of total process time.

The results for the aeroelastic kite are included in the diagrams in Figure 5. The angle of attack is measured as the angle between the freestream velocity **U** and the center chord line of the kite, as illustrated in Figure 3. The results show that the aerodynamic performance of the aeroelastic kite is better than that of the rigid pre-inflated kite. Both the lift is increased and the

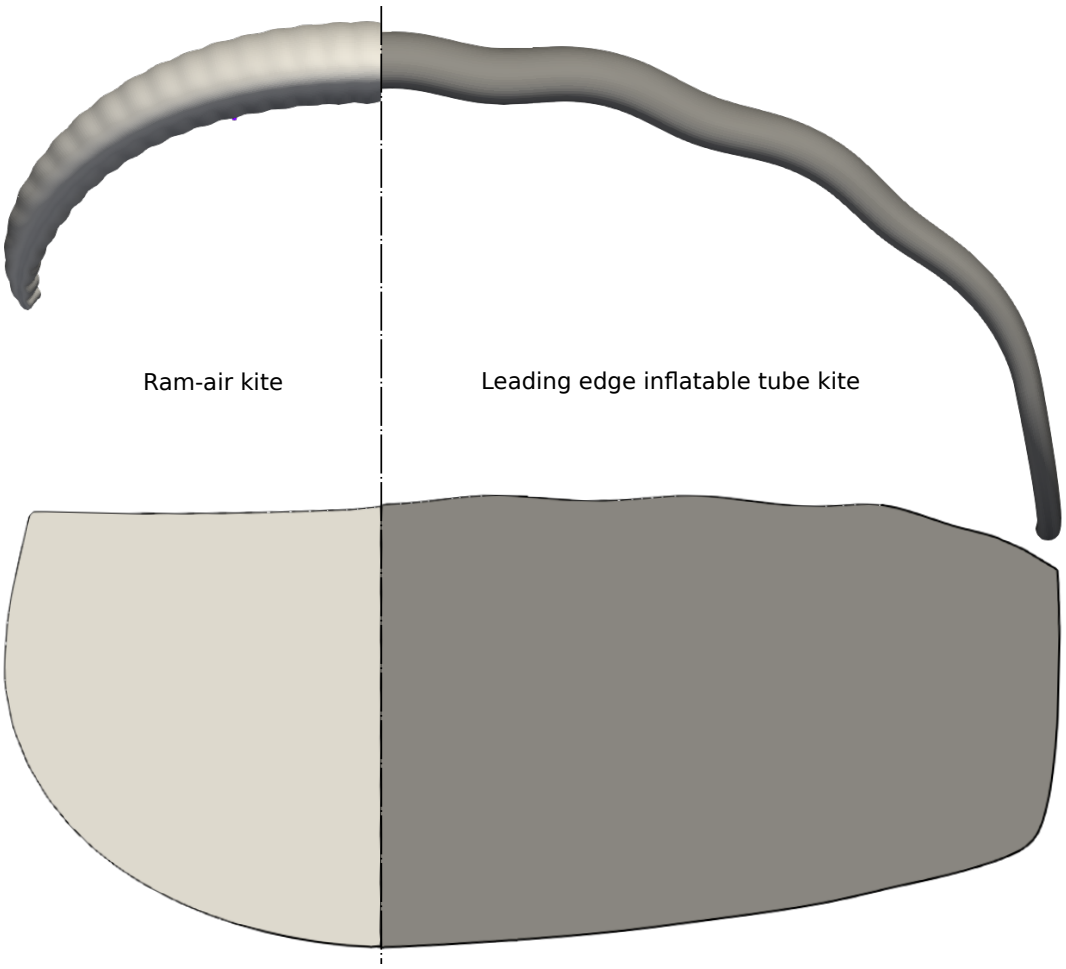

Figure 6. Front view (top) and planform view (bottom) of the pre-inflated ram-air kite investigated in this study and the LEI tube kite investigated by Viré et al. [20], fitted at the center chord.

drag is decreased resulting in a higher lift-to-drag ratio, which is commonly used as a measure for the aerodynamic performance of a wing. However, in airborne wind energy systems, the bridle lines and the tether create additional drag which favors high-lift wing designs to maintain a high overall aerodynamic performance of the system. In this work, the aerodynamic drag contribution of bridle lines and tether is not taken into account.

Figure 8 shows the cellular structure of the half wing, including the outlines of five representative ribs, for the pre-inflated and the aeroelastic kites, both at $\alpha = 18.5°$. Note that for the purpose of comparison, the aeroelastic kite is moved back to its initial position. For high angles of attack, the center of pressure moves towards the leading edge which shifts the aerodynamic load to the front bridle lines of each rib. This effect can also be observed in Figure 3, which shows that the two front bridle lines are taut while the two rear lines are more loose and for this reason deflected stronger by the aerodynamic drag. The high tension in the two front lines distorts the airfoil contour locally, generating two bumps at the line attachment points. In between the line attachments, the aerodynamic surface pressure indents the lower skin. The upper skin, on the other hand, is pulled away by the high suction pressure. Moreover, a rather planar region is formed at the stagnation region and the wingtips are bent forwards compared to the pre-inflated wing.

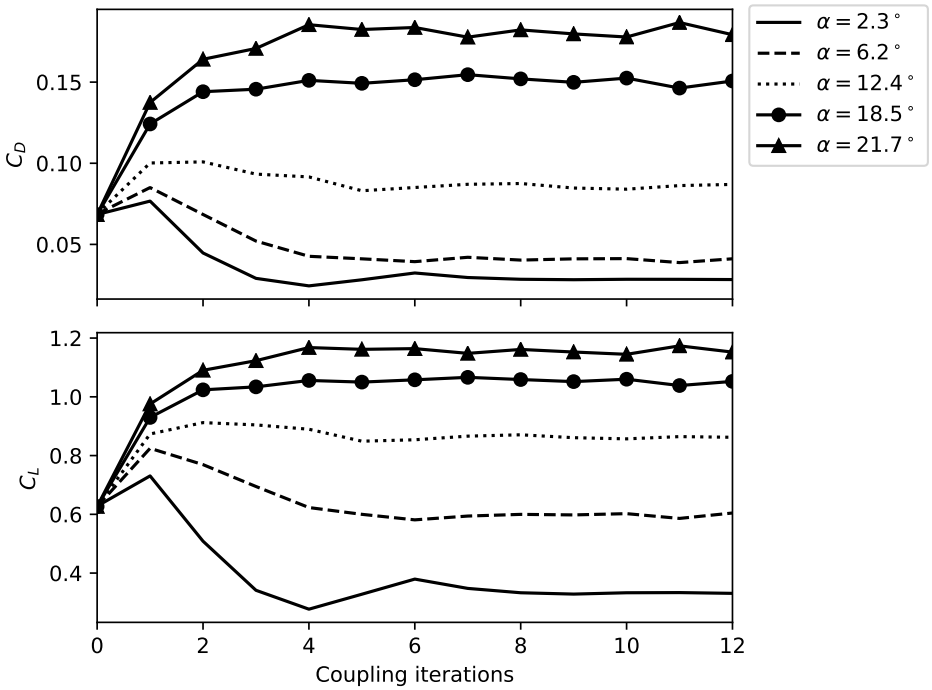

Figure 7. Evolution of the aerodynamic coefficients along the aeroelastic coupling iterations.

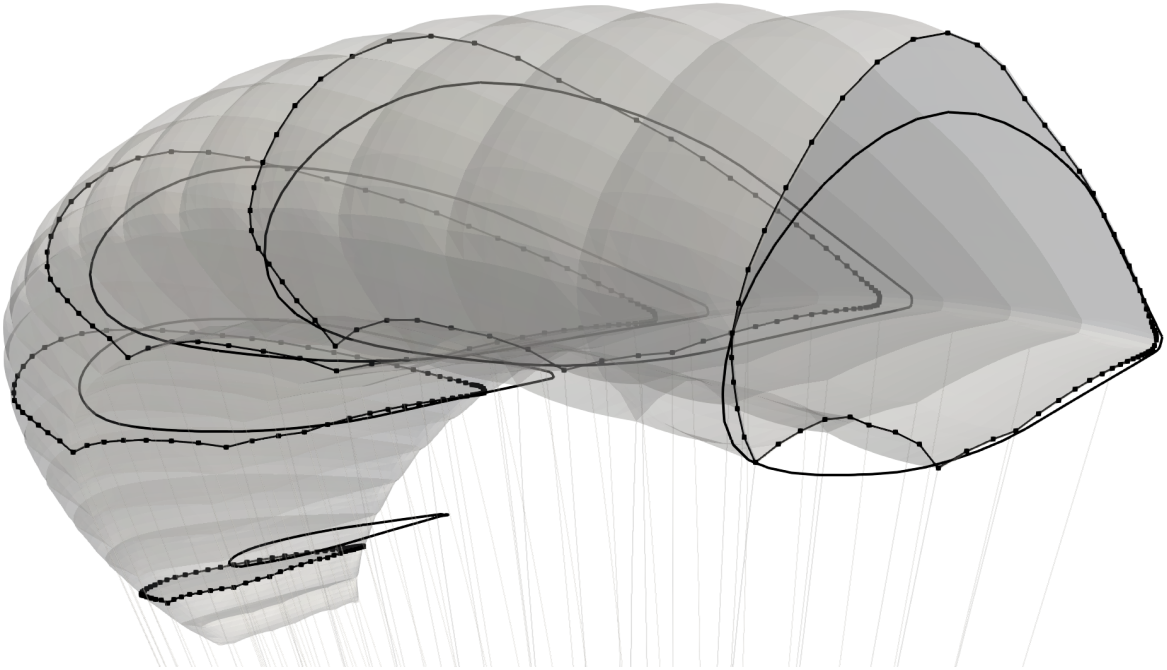

Figure 8. Half wing and five representative rib shapes for a steady-state angle of attack $\alpha = 18.5^\circ$. The rib shapes outlined by a solid line are for the pre-inflated rigid wing, while the rib shapes outlined by a line with dots are for the aeroelastic wing.

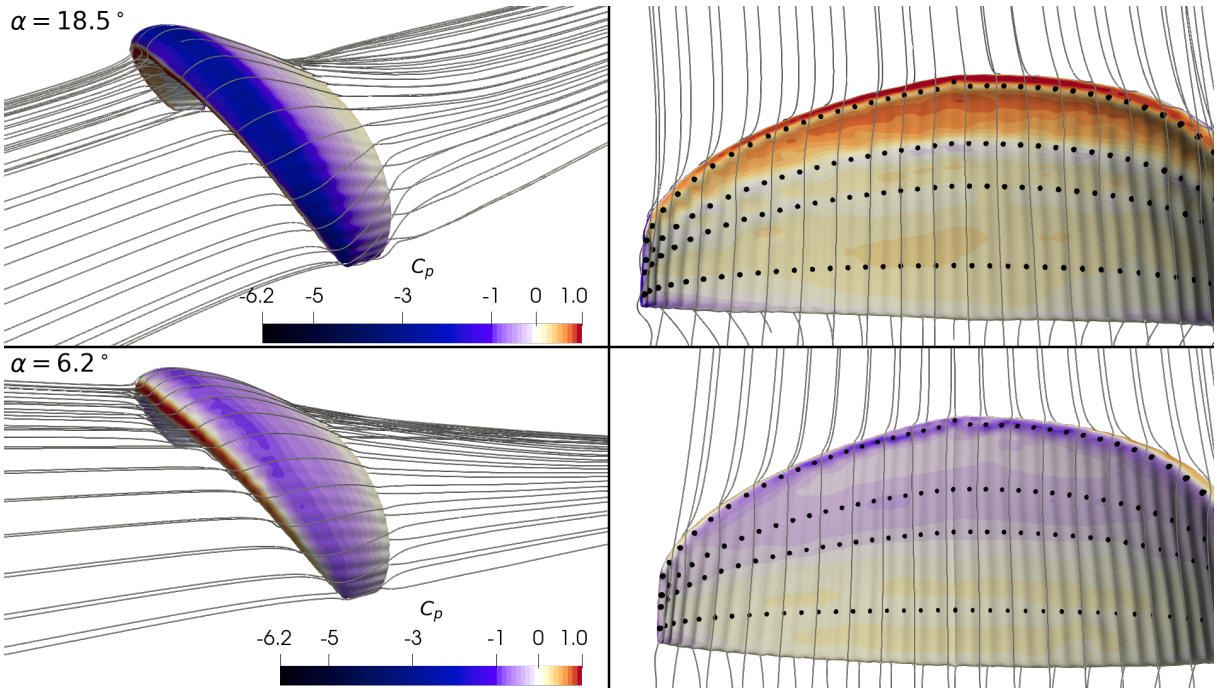

Figure 9. Streamlines along the wing and distribution of the surface pressure coefficient and bridle line attachment points on the wing surface.

Figure 9 shows the distribution of the pressure coefficient on the wing surface and the streamlines along the wing for two different angles of attacks. The bridle line attachment points on the lower skin are indicated by black dots. The pressure difference between lower and upper skin of the wing increases with the angle of attack, resulting in a stronger crossflow on the upper skin, pushing the streamlines towards the center. The lower skin does not indicate a significant crossflow, however, the bridle line attachment points clearly trace a rapid change in the streamwise pressure coefficient.

The bumpy profile and the resulting change in the pressure coefficient can be also seen in Figure 10 which shows the rib contour and the pressure coefficient in the symmetry plane. For the high angle of attack ($\alpha = 18.5°$), the surface pressure exhibits two local minima at the two front bridle lines. For the lower angles of attack also a third minima can be observed and the amplitudes exceed those for the high angle of attack. However, the pressure loss is approximately compensated by a higher pressure coefficient in between the bumps. The increase in pulling force with angle of attack is amplified by the increasing camber of the aeroelastic wing. On the other hand, an increasing angle of attack gradually shifts the peak camber towards the leading edge. The section lift and drag coefficients are listed in Table 4 for $\alpha = 18.5°$. We can conclude that the aeroelastic wing has higher lift and drag section coefficients than the rigid pre-inflated wing. The increased drag can be attributed to the bumpy lower skin while the higher lift can be attributed to the increased camber.

	α	c_d	c_l
Rigid pre-inflated	18.5°	0.13	0.87
Aeroelastic	18.5°	0.15	0.93

Table 4. Section aerodynamic coefficients at the symmetry plane rib

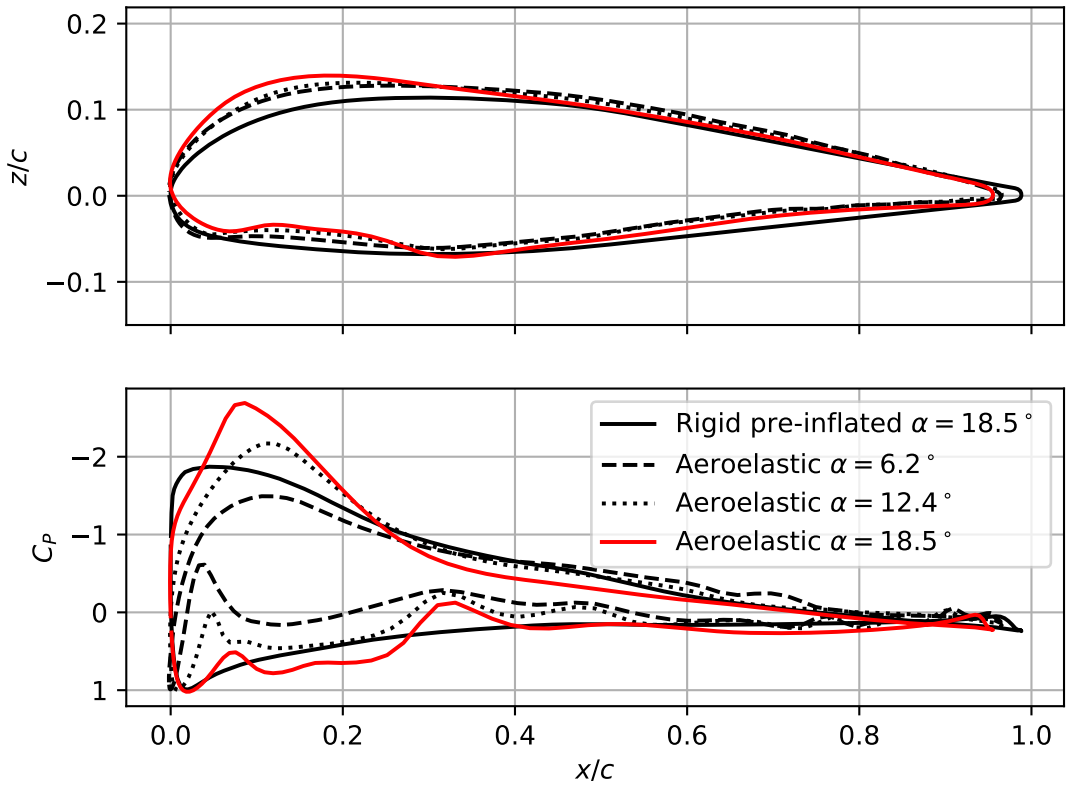

Figure 10. The symmetry plane wing contour (above) and the pressure coefficient distribution (below).

4. Conclusions

We developed a computational approach to simulate the steady-state aeroelastic deformation of a ram-air kite for airborne wind energy applications. The open source toolchain uses the coupling library preCICE to combine the CFD solver openFOAM for simulating the flow around the wing with the FE solver mem4py for simulating the deformation of the membrane structure. The tools used for meshing of the initial geometry are Cassiopee, PyHyp and cfMesh, while mesh deformation is handled with a radial basis function (RBF) method.

To assess the importance of aeroelasticity we compared a pre-inflated and then rigidized kite with a fully aeroelastic kite. The results show that the aeroelastic deformation of the cellular membrane structure and the bridle line system significantly affects the aerodynamic characteristics of the kite. The wing exhibits local deformation phenomena, such as billowing of the membrane or ballooning of the individual wing sections, as well as global deformation phenomena, such as spanwise contraction and bending. The flow field shows the typical flow phenomena for a wing with low aspect ratio and high anhedral angle, such as strong spanwise flow and distinct wingtip vortices.

The developed toolchain converges rapidly, is robust and capable of capturing the relevant physics of a wind energy harvesting ram-air wing. We consider the steady-state simulation framework to be a good compromise between model fidelity and computational cost and thus suitable to efficiently analyze and improve new kite designs. For future work, we propose to

ensure mesh independence of results and perform a thorough validation. Also, partitioned coupling schemes, which are already included in the preCICE coupling tool, could be used to accelerate the convergence of the coupling iterations.

Acknowledgements

This work is supported by the project AWESCO (H2020-ITN-642682) funded by the European Union's Horizon 2020 research and innovation programme under the Marie Skłodowska-Curie grant agreement No. 642682l. Roland Schmehl has received additional financial support by the project REACH (H2020-FTIPilot-691173), funded by the European Union's Horizon 2020 research and innovation programme under grant agreement No. 691173. The authors would like to thank SkySails Power for providing the CAD file of the ram-air wing and its bridle line system.

References

[1] H. Altmann. Fluid-structure interaction analysis of an isolated ram-air parafoil cell. In *AIAA Aviation 2019 Forum*, Dallas, Texas, 2019.
[2] C. Benoit, S. Peron, and Landier S. Cassiopee: a CFD pre- and post-processing tool. *Aerospace Science and Technology*, 45:272–283, 2015.
[3] D. Blom. `https://github.com/davidsblom/FOAM-FSI`. Accessed: 18 June 2020.
[4] M. Bungart. Fluid-Struktur Kopplung an einem RAM-Air-Kiteschirm. Master's thesis, University of Stuttgart, 2009.
[5] H. Bungartz, F. Lindner, B. Gatzhammer, M. Mehl, K. Scheufele, A. Shukaev, and B. Uekermann. preCICE – a fully parallel library for multi-physics surface coupling. *Computers and Fluids*, 141:250–258, 2016.
[6] Y. Cao and X. Zhu. Effects of characteristic geometric parameters on parafoil lift and drag. *Aircraft Engineering and Aerospace Technology*, 85(4):280–292, 2013.
[7] G Chourdakis and D Risseeuw. `https://github.com/precice/openfoam-adapter`. Accessed: 18 June 2020.
[8] A. de Wachter. Deformation and aerodynamic performance of a ram-air wing. Master's thesis, Delft University of Technology, 2008.
[9] P. Demkowicz. Numerical analysis of the flow past a leading edge inflatable kite wing using a correlation-based transition model. Master's thesis, Delft University of Technology, 2019.
[10] S. Dunker. Ram-air wing design considerations for airborne wind energy. In U. Ahrens, M. Diehl, and R. Schmehl, editors, *Airborne Wind Energy*, Green Energy and Technology, chapter 31, pages 517–546. Springer, Berlin Heidelberg, 2013.
[11] S. Dunker. Tether and bridle line drag in airborne wind energy applications. In R. Schmehl, editor, *Airborne Wind Energy – Advances in Technology Development and Research*, Green Energy and Technology, chapter 2, pages 29–56. Springer, Singapore, 2018.
[12] M Folkersma. `https://github.com/mfolkersma/RBFMeshDeformation`. Accessed: 22 June 2020.
[13] M. Folkersma, P. Thedens, R. Schmehl, and A. Vire. Fluid-structure interaction of inflatable wing section. In *Proceedings of the 8th International Conference on Coupled Problems in Science and Engineering*, 2019.
[14] H. Johari, O.A. Yakimenko, and T. Jann. Aerodynamic characterization of parafoils. In Oleg A. Yakimenko, editor, *Precision Aerial Delivery Systems: Modeling, Dynamics, and Control, Progress in Astronautics and Aeronautics*, chapter 4, pages 199–264. AIAA, 2014.
[15] T. Lolies, N. Gourdain, M. Charlotte, H. Belloc, and B. Goldsmith. Numerical methods for efficient fluid–structure interaction simulations of paragliders. *Aerotecnica Missili & Spazio*, 98:221–229, 2019.
[16] X. Paulig, M. Bungart, and B. Specht. Conceptual design of textile kites considering overall system performance. In U. Ahrens, M. Diehl, and R. Schmehl, editors, *Airborne Wind Energy*, Green Energy and Technology, chapter 32, pages 547–562. Springer, Berlin Heidelberg, 2013.
[17] pyHyp. `https://github.com/mdolab/pyhyp`. Accessed: 02 March 2020.
[18] P Thedens. `https://github.com/pthedens/mem4py`. Accessed: 18 June 2020.
[19] P. Thedens, G. de Oliveira, and R. Schmehl. Ram-air kite airfoil and reinforcements optimization for airborne wind energy applications. *Wind Energy*, 22(5):653–665, 2019.
[20] A Viré, P. Demkowicz, M.A.M. Folkersma, A. Roullier, and R. Schmehl. Reynolds-averaged Navier-Stokes simulations for flow past a leading edge inflatable wing for airborne wind energy applications. In *Proceedings of the Torque 2020 conference*, Delft, The Netherlands, 2020.